This paper appeared in Proceedings of the SPIE Conference on Algorithms for SAR Imagery IX, vol. 4727, Orlando, FL, April 2002.

Analysis of the Impact of Feature-Enhanced SAR Imaging on ATR Performance

Müjdat Çetin[a], William C. Karl[b], and David A. Castañon[b]

[a]Laboratory for Information and Decision Systems, Massachusetts Institute of Technology, 77 Massachusetts Ave., Cambridge, MA 02139, USA

[b]Multi-Dimensional Signal Processing Laboratory, Boston University, 8 Saint Mary's St., Boston, MA 02215, USA

ABSTRACT

We present an evaluation of the impact of a recently proposed feature-enhanced synthetic aperture radar (SAR) imaging technique on automatic target recognition (ATR) performance. We run recognition experiments using conventional and feature-enhanced SAR images of military targets, in three different classifiers. The first classifier is template-based. The second classifier makes a decision through a likelihood test, based on Gaussian models for reflectivities. The third classifier is based on extracted locations of the dominant target scatterers. The experimental results demonstrate that feature-enhanced SAR imaging can improve the recognition performance, especially in scenarios involving reduced data quality or quantity.

Keywords: Synthetic aperture radar, automatic target recognition, image reconstruction, non-quadratic regularization, feature-enhanced imaging, superresolution, classification.

1. INTRODUCTION

Recently a novel technique for synthetic aperture radar (SAR) image formation based on non-quadratic regularization has been proposed.[1] This method can preserve and enhance target features better than conventional images. This feature-enhanced SAR imaging technique has been quantitatively evaluated based on recognition-oriented features in Ref. 2. In particular, that study has shown that images produced by feature-enhanced imaging exhibit higher resolution and better dominant scatterer localization than conventional images; as well as enhanced anomaly and speckle suppression in homogeneous regions, which results in easier-to-segment images. The question of how such feature-enhanced imaging affects automatic target recognition (ATR) performance was not addressed.

In this work, we present an evaluation of the impact of feature-enhanced SAR imaging on ATR performance. We use the Moving and Stationary Target Acquisition and Recognition (MSTAR) public target data set,[3] and three different classifiers, to make decisions about the target type given conventional or feature-enhanced images, and compare the results for these two types of images. The first classifier is based on template-matching, which is a conventional approach for SAR ATR. The second classifier is based on conditionally Gaussian models for reflectivities, and performs classification through a likelihood test. The third classifier is a feature-based one, and performs classification by measuring how well the dominant scatterer locations extracted from images formed from reduced-resolution data match the corresponding scatterer locations for each hypothesized target. We present the recognition results in the form of classifier confusion matrices. These experiments demonstrate that feature-enhanced SAR imaging can offer higher probability of correct classification than conventional imaging.

Further author information: (Send correspondence to M.Ç.)
M.Ç.: E-mail: mcetin@mit.edu
W.C.K.: E-mail: wckarl@bu.edu
D.A.C.: E-mail: dac@bu.edu

2. FEATURE-ENHANCED SAR IMAGING

In this section, we provide a brief overview of feature-enhanced SAR image formation. The details of the technique can be found in Ref. 1. Let us start from the following assumed discrete model for the SAR observation process:

$$\mathbf{g} = \mathbf{T}\mathbf{f} + \mathbf{w} \tag{1}$$

where $\mathbf{g}$ are the SAR observations (phase histories or range profiles), $\mathbf{f}$ is the unknown sampled reflectivity image, $\mathbf{w}$ is additive measurement noise, all column stacked as vectors, and $\mathbf{T}$ is a complex-valued SAR observation matrix. If phase history data are used, $\mathbf{T}$ is a 2-D Fourier-type operator,[4] and if range profile data are used, $\mathbf{T}$ is a complex-valued projection-type operator. In this framework, the objective of SAR image reconstruction is to obtain an estimate of $\mathbf{f}$ based on the data $\mathbf{g}$. The conventional SAR polar format image formation algorithm can roughly be interpreted in this framework as the application of the adjoint to the data: $\hat{\mathbf{f}}_{\mathrm{CONV}} = \mathbf{T}^H\mathbf{g}$.

In contrast, feature-enhanced SAR image reconstruction is achieved by solving an optimization problem of the following form:

$$\hat{\mathbf{f}} = \arg\min_{\mathbf{f}} \left[\|\mathbf{g} - \mathbf{T}\mathbf{f}\|_2^2 + \lambda_1 \|\mathbf{f}\|_p^p + \lambda_2 \|\mathbf{D}|\mathbf{f}|\|_p^p \right] \tag{2}$$

where $\|\cdot\|_p$ denotes the ℓ_p norm ($p \leq 1$), $\mathbf{D}$ is a 2-D derivative operator, $|\mathbf{f}|$ denotes the vector of magnitudes of the complex-valued vector $\mathbf{f}$, and λ_1, λ_2 are scalar parameters. The first term in the objective function of Eq. (2) is a data fidelity term. The second and third terms in Eq. (2) incorporate prior information regarding both the behavior of the field $\mathbf{f}$, and the nature of the features of interest in the resulting reconstructions. The optimization problem in Eq. (2) can be solved by using an efficient iterative algorithm proposed in Ref. 1, based on half-quadratic regularization.[5] Use of non-quadratic constraints, such as those in Eq. (2), has recently become popular, e.g. in image restoration,[6] due to the ability of these constraints to prevent suppression of useful features in the image. The objective function in Eq. (2) extends the use of such constraints to the complex-valued SAR image reconstruction problem.

Each of the last two terms in Eq. (2) is aimed at enhancing a particular type of feature that is of importance for SAR ATR. In particular, the term $\|\mathbf{f}\|_p^p$ is an energy-type constraint on the solution, and aims to suppress artifacts and increase the resolvability of *point* scatterers. The $\|\mathbf{D}|\mathbf{f}|\|_p^p$ term on the other hand, aims to reduce variability in homogeneous *regions*. The relative magnitudes of λ_1 and λ_2 determine the emphasis on such *point-based* versus *region-based* features. Therefore, this framework lets us reconstruct images with two different flavors: using a relatively large λ_1 yields *point-enhanced* imagery, and using a relatively large λ_2 yields *region-enhanced* imagery. For point-enhanced imaging, when the observation model $\mathbf{T}$ maps a high-resolution field to lower-resolution data, we call this *superresolution* imaging, since in this case we attempt to reconstruct the field at a finer pixel-spacing than Rayleigh resolution. When this is not the case, we use the term *non-superresolution* imaging. The superresolving capabilities of feature-enhanced SAR imaging have been studied in Ref. 2.

3. CLASSIFIERS USED FOR ATR

In this section, we describe the three classifiers we use for evaluating the impact of feature-enhanced SAR imaging on the success of ATR. The first of these is a template-based classifier, which can be considered as a conventional SAR ATR approach. The second classifier achieves a decision through a likelihood test on the observed target images based on Gaussian models for the reflectivities parameterized by the target class. The third one, a point-feature-based classifier, is based on measuring how well features (dominant scatter locations) extracted from images reconstructed from low resolution data match those of the hypothesized target class.

3.1. Template-based Classifier

The idea in template-based classification is to first measure how well a given test image matches reference images, called templates, which represent the hypotheses in the problem, and then declare the test image to be from the class giving the best matching score. A common metric used for the degree of match is the mean-squared error (MSE) between the test image, and the template. This classification approach has been used in the classifier component of a series of ATR systems developed by Lincoln Laboratory.[7,8]

The classification problem in ATR is to determine the type of the vehicle in a given scene. In SAR, the image of a particular type of vehicle at a particular orientation (aspect angle) with respect to the radar platform is usually not equivalent to a rotated version of the image of the same vehicle at a significantly different orientation. Hence for template-based classification, we need templates of the targets at a reasonable number of different orientations. Let $\mathbf{t}(\vartheta, a)$ be such a template (stacked as a vector) for vehicle type a, at orientation $\vartheta \in [0°, 360°)$, and let $\hat{\mathbf{f}}_{\mathrm{dB}}$ be a normalized (to have unit ℓ_2-norm) test image (in dB) stacked as a vector. Then the template-based minimum MSE classification can be done as follows:

$$\hat{a}_{\mathrm{MSE}} = \arg\min_{a} \left(\min_{\vartheta} \|\hat{\mathbf{f}}_{\mathrm{dB}} - \mathbf{t}(\vartheta, a)\|_2^2 \right). \tag{3}$$

The classifier in Eq. (3) needs a stored set of templates, which in practice can be obtained from training data. In practice, we usually do not have many training images at exactly the same orientation. Then, the template for vehicle type a, at orientation ϑ_k can be constructed by first aligning (in angle) the training images that have an orientation close to ϑ_k, and then finding an average of these images, as follows:

$$\mathbf{t}(\vartheta_k, a) = \frac{1}{N_k} \sum_{\vartheta \in W_k} \hat{\mathbf{f}}_{\mathrm{dB}}^{r_k}(\vartheta, a) \tag{4}$$

where W_k denotes the range of angular orientations that are used in training for the orientation ϑ_k, N_k is the number of available training images that have an orientation within this range, and $\hat{\mathbf{f}}_{\mathrm{dB}}^{r_k}(\vartheta, a)$ is a training image which has an original orientation of ϑ, and which is rotated $\vartheta_k - \vartheta$ degrees, so that it is aligned with other training images used for the computation of $\mathbf{t}(\vartheta_k, a)$. Such templates for T72 tanks from the MSTAR data set, at 17° depression angle and various orientations for the conventional, point-enhanced (non-superresolution), and region-enhanced images are shown in Figures 1, 2, and 3. The orientation ϑ for each image used in the computation of these templates is obtained from the corresponding MSTAR file header. In the construction of these templates, we have used $\vartheta_k = 5(k-1)$ degrees, and $W_k = [\vartheta_k - 5, \vartheta_k + 5)$, where $k \in \{1, 2, ..., 72\}$. Hence the sets of images used in the computation of templates for subsequent orientations intersect each other, and each training image is used in the construction of two templates. In our experimental work, described in Section 4, we use images at 17° depression angle for training the classifiers, and an independent set of images at 15° depression angle to test the classification performance.

3.2. Likelihood-based Classifier

We now describe a likelihood-based classifier, proposed in Ref. 9 for SAR ATR. This approach starts from a statistical signal model, in which the underlying SAR image $\mathbf{f}(\vartheta, a)$, where ϑ and a are as defined in Section 3.1, is assumed to be a complex Gaussian vector, and the observed image $\hat{\mathbf{f}}$ is given by the following observation model:

$$\hat{\mathbf{f}} = \mathbf{f}(\vartheta, a) + \mathbf{n} \tag{5}$$

where $\mathbf{n}$ is i.i.d. complex Gaussian noise with mean $\mathbf{0}$ and covariance $\sigma^2\mathbf{I}$. The classifier is based on a generalized likelihood test as follows:

$$\hat{a}_{\mathrm{GLRT}} = \arg\max_{a} \left(\max_{\vartheta} l(\hat{\mathbf{f}}|\vartheta, a) \right) \tag{6}$$

where $l(\hat{\mathbf{f}}|\vartheta, a)$ denotes the logarithm of the likelihood that the test image is of target type a, at orientation ϑ. Let the signal $\mathbf{f}(\vartheta, a)$ have mean $\mathbf{m}(\vartheta, a)$ and covariance $\mathbf{Q}(\vartheta, a)$. Then the probability density function $p(\hat{\mathbf{f}}|\vartheta, a)$ is Gaussian with the following mean and covariance:

$$E\{\hat{\mathbf{f}}|\vartheta, a\} = \mathbf{m}(\vartheta, a) \tag{7}$$

$$E\{[\hat{\mathbf{f}} - \mathbf{m}][\hat{\mathbf{f}} - \mathbf{m}]^H|\vartheta, a\} = \mathbf{Q}(\vartheta, a) + \sigma^2\mathbf{I}. \tag{8}$$

Let us define $\mathbf{K}(\vartheta, a) \triangleq \mathbf{Q}(\vartheta, a) + \sigma^2\mathbf{I}$. Then the log-likelihood is given by:

$$l(\hat{\mathbf{f}}|\vartheta, a) \propto -\log|\mathbf{K}(\vartheta, a)| - [\hat{\mathbf{f}} - \mathbf{m}(\vartheta, a)]^H (\mathbf{K}(\vartheta, a))^{-1} [\hat{\mathbf{f}} - \mathbf{m}(\vartheta, a)]. \tag{9}$$

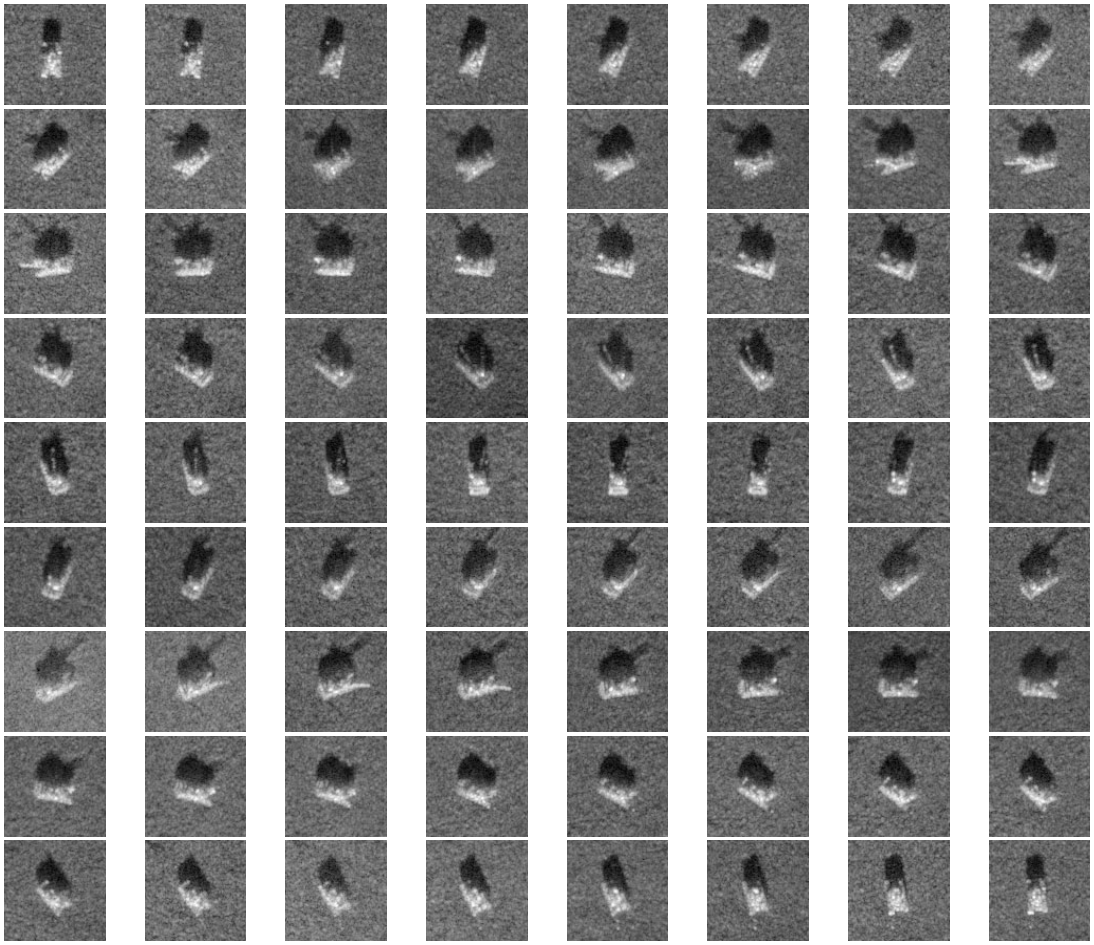

Figure 1. Conventional templates for the T72 target at 17° depression angle. Each image shows the template for a different aspect angle, starting from 0° on the top left, and covering all 360° with 5° increments, and a 10° window for averaging.

We assume that $\mathbf{m}(\vartheta, a) = \mathbf{0}$, $\forall\{\vartheta, a\}$, as in Ref. 9. This is a reasonable assumption due to the random phase nature of SAR reflectivities. The second simplifying assumption made in Ref. 9 is that of statistical independence of different pixels in the SAR image, which results in a diagonal $\mathbf{Q}(\vartheta, a)$, hence a diagonal $\mathbf{K}(\vartheta, a)$. This in turn simplifies the computation of the likelihood to a simple summation:

$$l(\hat{\mathbf{f}}|\vartheta, a) \propto \sum_i \left[-\log(\mathbf{K}_{i,i}(\vartheta, a)) - \frac{|(\hat{\mathbf{f}})_i|^2}{\mathbf{K}_{i,i}(\vartheta, a)} \right] \tag{10}$$

where $(\cdot)_i$ and $(\cdot)_{i,i}$ denote the i-th element of a vector, and the i-th diagonal element of a matrix respectively. The classifier in Eq. (6) with the likelihood function in Eq. (10) requires the model variances $\mathbf{K}_{i,i}(\vartheta, a)$. These variances can be estimated from training data as follows:

$$\mathbf{K}_{ii}(\vartheta_k, a) = \frac{1}{N_k} \sum_{\vartheta \in W_k} \left| \left(\hat{\mathbf{f}}^{r_k}(\vartheta, a) \right)_i \right|^2 \tag{11}$$

where $(\hat{\mathbf{f}}^{r_k}(\vartheta, a))_i$ denotes the i-th pixel of an aligned training image, and N_k, W_k are as defined in Section 3.1. The operation in Eq. (11) produces variance "images", which are, in spirit, very similar to the template images

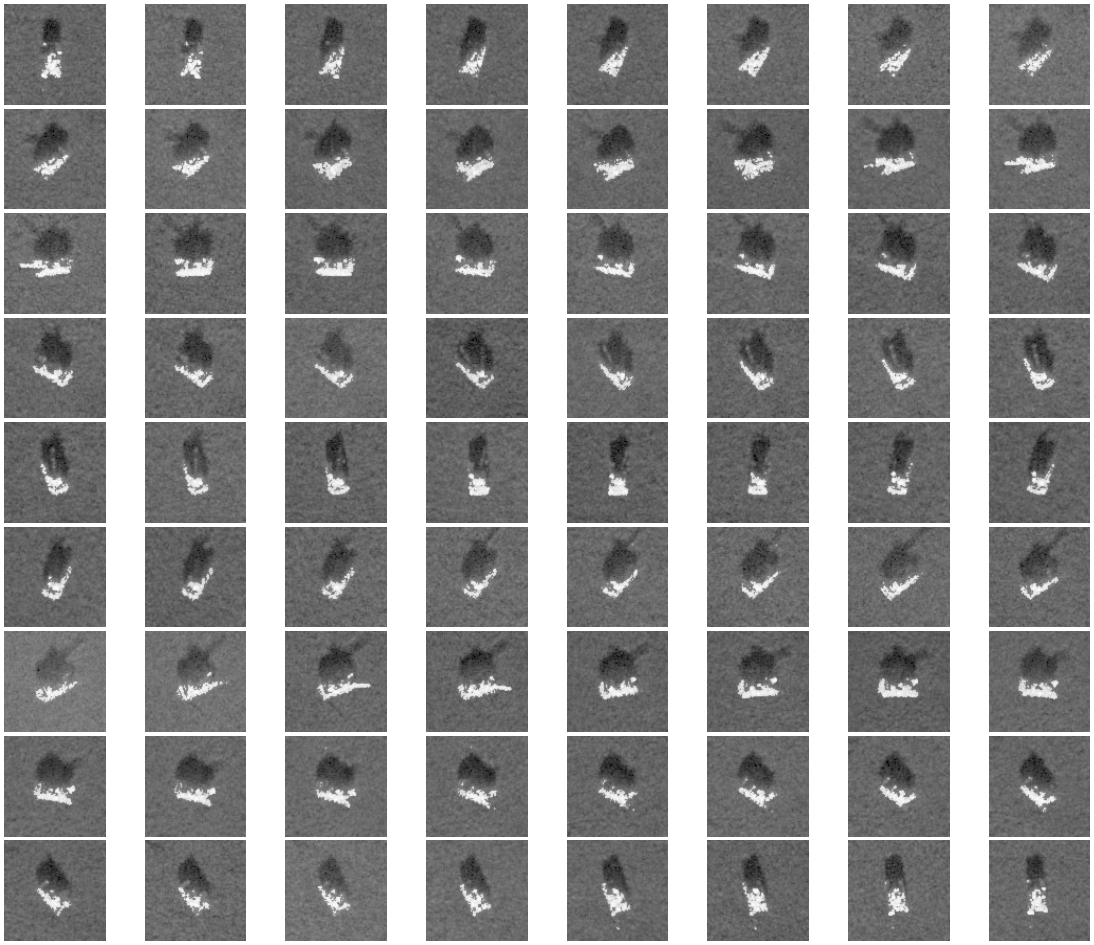

Figure 2. Point-enhanced templates for the T72 target at 17° depression angle. Each image shows the template for a different aspect angle, starting from 0° on the top left, and covering all 360° with 5° increments, and a 10° window for averaging.

of Figures 1, 2, and 3.

3.3. Point-feature-based Classifier

We now concentrate on the reconstruction problem from reduced-resolution data, and propose a classifier specifically aimed at evaluating the ability of the point-enhanced, superresolution images to preserve the locations of dominant scatterers in the scene. Similar peak-based classification schemes have previously been proposed in Refs. 10 and 11. Such feature-based classification techniques, as opposed to the pixel-based classification schemes described in Sections 3.1 and 3.2, have been an important component of recent research efforts such as those in DARPA's Moving and Stationary Target Acquisition and Recognition (MSTAR) program.[11]

The classifier works as follows. Given a test image, the first step is to extract the locations of the N_p brightest scatterers. For this purpose, we first find all the peaks in the scene. The peaks are taken to be the points where the discrete spatial derivatives of the reflectivity magnitude in both the x and the y directions change sign from positive to negative. Once the peaks are found, we order them based on their magnitudes, and pick the largest N_p of them. Once the N_p dominant peaks are extracted, a one-to-one association is established between these peaks and the true peak locations for the hypothesis under test. A one-to-one association of the peaks is made such that the sum of the squared distances between the locations of the true peaks and the

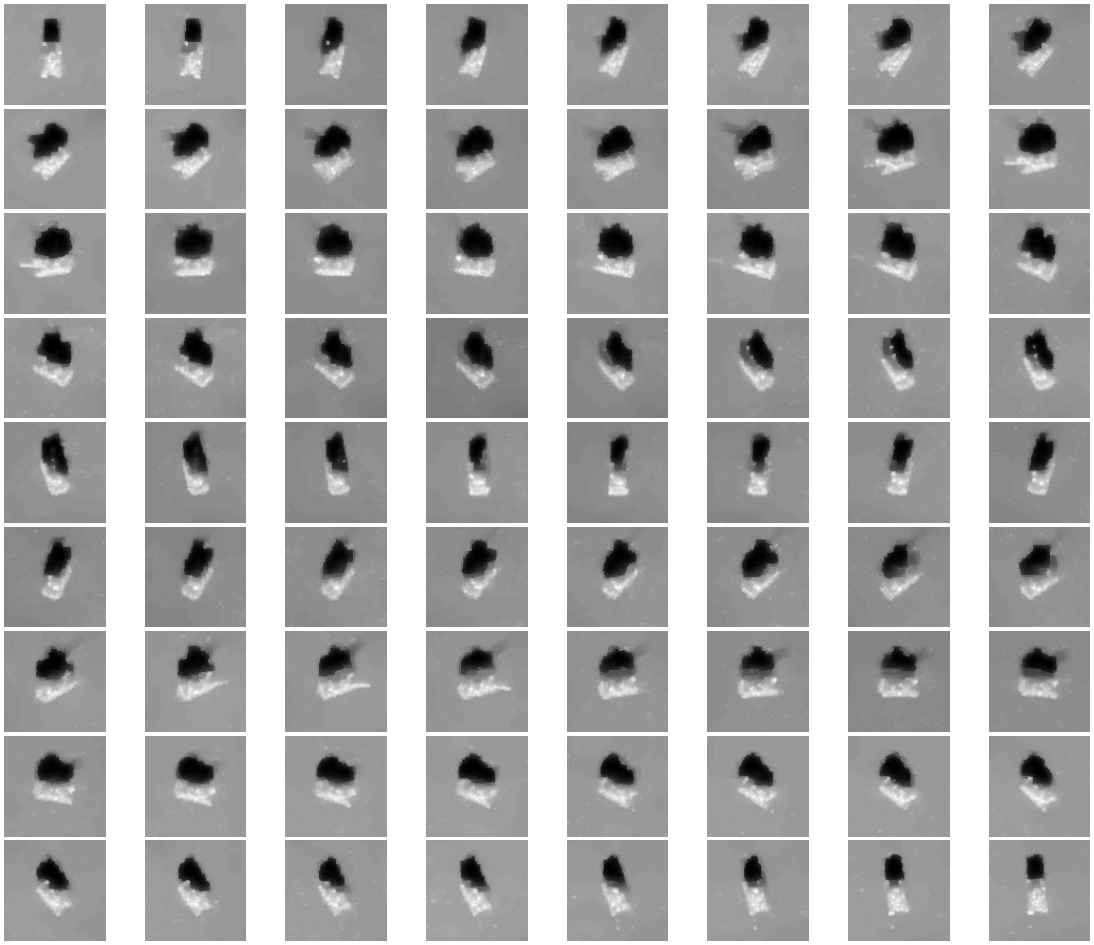

Figure 3. Region-enhanced templates for the T72 target at 17° depression angle. Each image shows the template for a different aspect angle, starting from 0° on the top left, and covering all 360° with 5° increments, and a 10° window for averaging.

corresponding matched peaks from the test image is minimized. Next, an average of the distances between the associated peak pairs is computed. This gives a single number measuring how likely it is that the given test image belongs to the hypothesized class. The class assignment is achieved by finding the vehicle type which yields the minimum associated peak distance over all orientations:

$$\hat{a}_{\text{PEAK}} = \arg\min_{a} \left(\min_{\vartheta} \frac{1}{N_p} \|\mathbf{d}_{\text{PEAK}}(\hat{\mathbf{f}}, \mathbf{f}(\vartheta, a))\|_1 \right) \tag{12}$$

where $\mathbf{d}_{\text{PEAK}}(\cdot,\cdot)$ is a vector of Euclidean distances between associated peak pairs extracted from the observed test image $\hat{\mathbf{f}}$, and the reference image $\mathbf{f}(\vartheta, a)$. Note that the ℓ_1-norm in Eq. (12) is just equivalent to a summation of the distances between individual peak pairs. The classifier in Eq. (12) requires the "true" peak locations for each target type, at a reasonable number of orientations ϑ, extracted from the reference scenes $\mathbf{f}(\vartheta, a)$. One way to obtain the reference peak locations is through the use of 3-D CAD models of the vehicles together with an electromagnetic signature prediction tool such as XPATCH[12] to simulate the expected reference scene. A second option is to use conventional SAR images obtained from higher resolution data as the reference scenes, and extract the "true" peak locations from such images. In our experiments, we use the latter approach.

	Training set		Test set	
Target	Depression	No. of images	Depression	No. of images
T72	17°	232	15°	196
BMP2	17°	233	15°	195
BTR70	17°	233	15°	196

Table 1: Composition of the MSTAR data set used in recognition experiments.

4. EXPERIMENTAL RESULTS

4.1. Experimental Setup

We now evaluate the performance of the classifiers described in the previous sections, given MSTAR images produced by feature-enhanced versus conventional imaging. The MSTAR data set consists of a large assortment of military targets. In our recognition experiments, we use the T72, BMP2 and BTR70 targets. For all three classifiers, our training set is composed of images at 17° depression angle, and our test set is composed of an independent set of images at 15° depression angle. The numbers of each type of target images in each of these sets are shown in Table 1. In training and testing with all three classifiers, we extract and use a near-central portion of the SAR image which contains the target. In all cases, we normalize the images so that they have the same ℓ_2-norm, before using them in the classifiers.

We present the results of our evaluations in the form of classifier confusion matrices, which show the number of correct and incorrect classifications achieved on test inputs of each type. A single number characterizing the classifier's ability to recognize test inputs can be obtained through the probability of correct classification, P_{cc}, which is defined as the fraction of all target test inputs that were correctly classified.

4.2. Template-based Classification Results

We now present the recognition performance of the conventional, point-enhanced (non-superresolution) and region-enhanced images, when they are used as inputs to the template-based classifier, described in Section 3.1. We use 72 templates for each target type, with each template representing an orientation 5° apart from the subsequent template. In the construction of each template, we use a training window W_k of 10 degrees, as described in Section 3.1.

We have initially conducted recognition experiments with images reconstructed from high SNR data. By high SNR data, we mean the SAR data obtained by undoing the image formation steps for the images in the MSTAR data set, without any additional measurement noise. The templates for such images were shown in Figures 1, 2, 3. We have observed that for this high-SNR, 3-target classification problem both conventional and feature-enhanced images result in a high recognition rate, and the performance difference is not significant. Next, we investigate the recognition performance of these images in the face of degraded data, which may provide a better representation of a practical situation. To this end, we have included additive complex Gaussian noise in the projectional SAR data. Treating the original data before the addition of this noise as the clean signal, the SNR of the corrupted data we use is -4 dB. This represents a very noisy scenario. The templates of the T72 target for the conventional and feature-enhanced images in this case are shown in Figures 4, 5, and 6.

We now present the recognition results for this low-SNR case. Table 2 shows the confusion matrices for the classification of conventional and feature-enhanced images. The conventional images result in an overall probability of correct classification of 69.85 %. Point-enhanced and region-enhanced imaging increase this rate to 88.93 % and 96.76 % respectively. So degradation in recognition performance caused by the noise is much less with the feature-enhanced images, as compared to the conventional images. Hence feature-enhanced imaging is more robust to limitations in data quality.

4.3. Likelihood-based Classification Results

We now present the results of running the low-SNR data used in Section 4.2 through the likelihood-based classifier described in Section 3.2. For each target type, we train 72 probability density functions, each representing

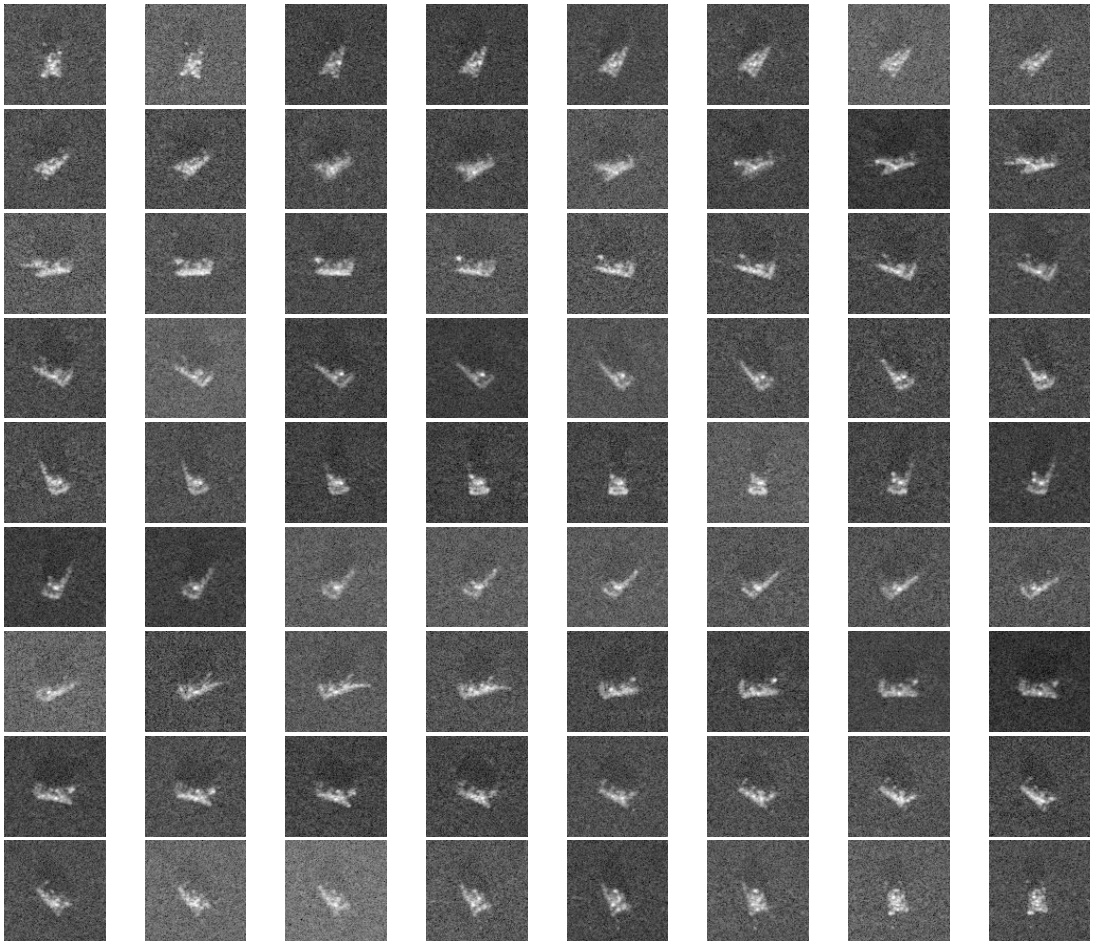

Figure 4. Conventional templates for the T72 target at 17° depression angle, reconstructed from low-SNR data. Each image shows the template for a different aspect angle, starting from 0° on the top left, and covering all 360° with 5° increments, and a 10° window for averaging.

an orientation 5° apart from the subsequent orientation. As in the construction of the templates in Section 4.2, we use a training window W_k of 10 degrees, in estimating the covariance matrices.

The classification results are shown in Table 3. The classifier has a correct classification rate of 87.05 % with conventional images, 94.38 % with point-enhanced images, and 99.15 % with region-enhanced images.

4.4. Point-feature-based Classification Results

We now report the results of recognition experiments with images reconstructed from data supporting a lower resolution than those used in the previous recognition tests in this paper. The data used in Sections 4.2 and 4.3 had a resolution of 0.3 m. In this section, we use data with a resolution of 0.6 m. The data used for the low resolution experiments do not contain any noise in addition to what is already present in the MSTAR data. Hence, we consider a high-SNR scenario here.

We could certainly use a template-based, or likelihood-based classifier for the images reconstructed from such data as well. However, our objective in this section is to present the results of a feature-based classification scheme, rather than a pixel-based one. The classifier we use has been described in Section 3.3. We obtain the true peak locations for all targets at all the orientations available, using conventionally formed SAR images

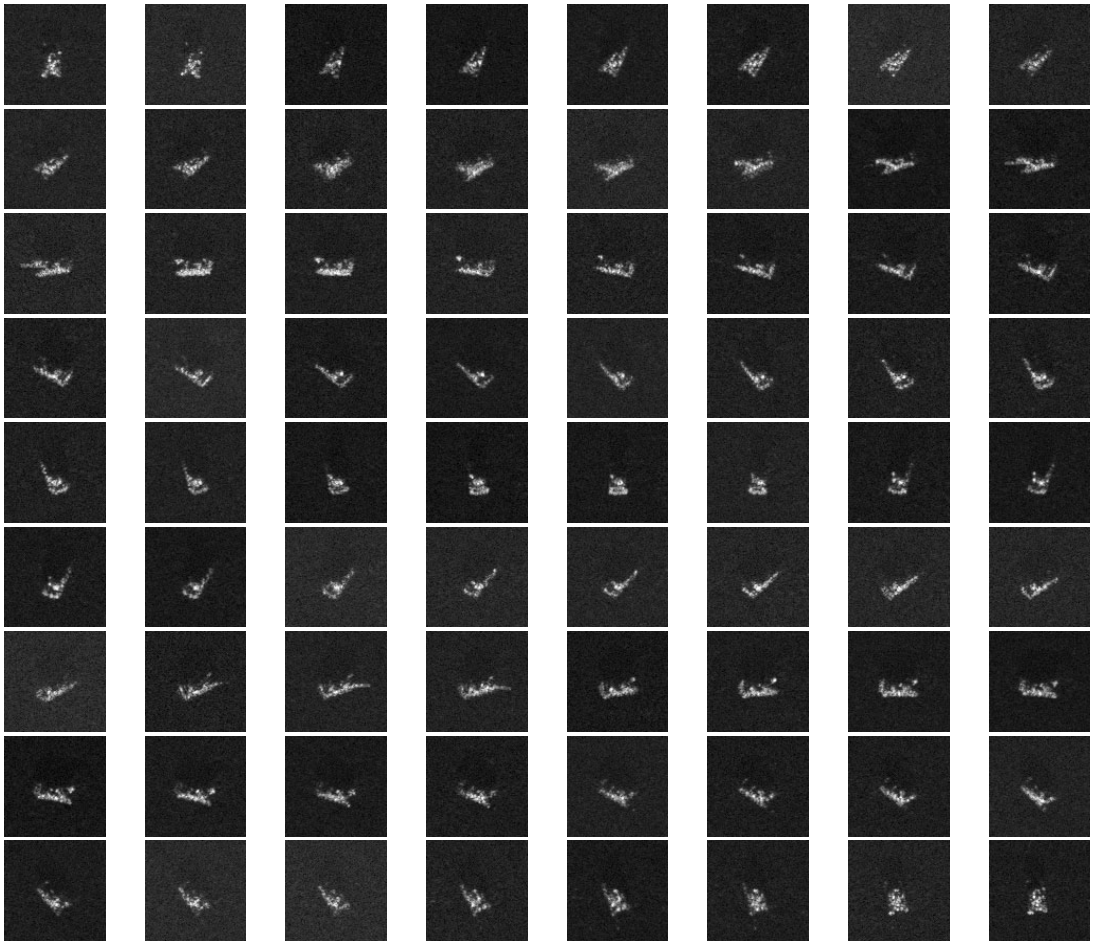

Figure 5. Point-enhanced templates for the T72 target at 17° depression angle, reconstructed from low-SNR data. Each image shows the template for a different aspect angle, starting from 0° on the top left, and covering all 360° with 5° increments, and a 10° window for averaging.

at 0.3 m resolution, and 17° depression angle. We then run the classifier on conventional and point-enhanced, superresolution images at 15° depression angle, reconstructed from data supporting a resolution of 0.6 m. The number of dominant scatterers we consider for each image is $N_p = 20$.

The classification results presented in Table 4 demonstrate a clear improvement in recognition performance through the use of point-enhanced, superresolution images as compared to the case of conventional images. The correct classification rates for the conventional and point-enhanced images are 44.80 %, and 81.43 %, respectively.

5. FURTHER ANALYSIS AND EXTENSIONS

We have presented some recognition experiments to compare the performance of feature-enhanced and conventional images. Although this analysis has provided a flavor of the impact of feature-enhanced imaging, more extensive experimentation on a more general setting would be an important contribution for a number of reasons. First, the recognition problem posed in this paper contained three classes. This is too small to represent a practical setting where the decisions usually involve a larger number of vehicle types. Furthermore, our experiments did not involve *confuser* vehicles. Confuser vehicles are test inputs, for which no training is done, and the ATR system should ideally respond as "unknown" to data containing such vehicles. This is an

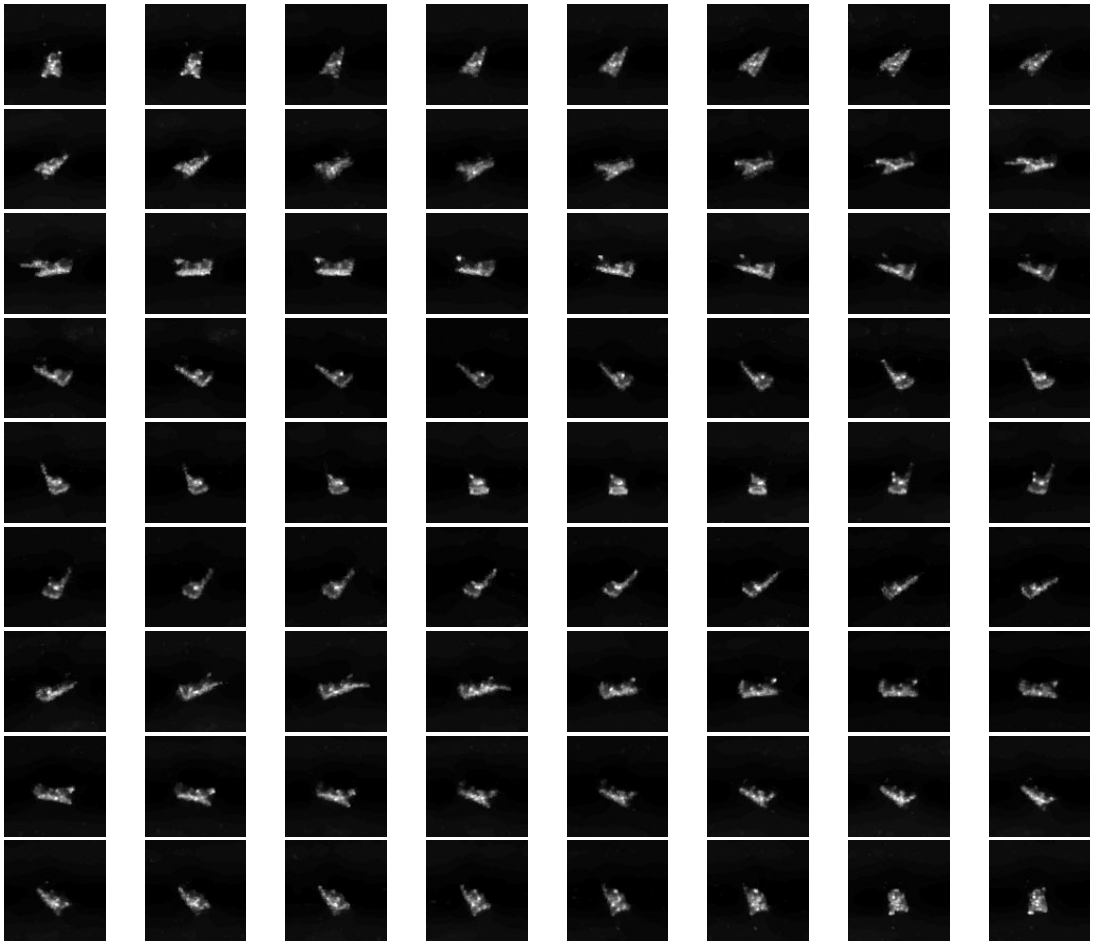

Figure 6. Region-enhanced templates for the T72 target at 17° depression angle, reconstructed from low-SNR data. Each image shows the template for a different aspect angle, starting from 0° on the top left, and covering all 360° with 5° increments, and a 10° window for averaging.

important practical issue, and a more realistic recognition evaluation should involve confuser vehicles. Finally, although the pixel-based classifiers that we considered were based on real recognition systems in use, there are more advanced, feature-based systems under development, such as that associated with the MSTAR program, as described in Ref. 11. Evaluation of the performance of feature-enhanced SAR images in such a feature-based recognition system would be an important extension of the work presented in this paper.

6. CONCLUSIONS

We have conducted a preliminary analysis of the impact of feature-enhanced SAR imaging on ATR performance. We have defined a 3-class target recognition problem to compare the recognition performance of feature-enhanced images and conventional images. We have constructed two pixel-based classifiers, and one feature-based classifier. With high-SNR data we have not observed a significant performance difference between the conventional and the feature-enhanced images. With reduced quality data however, feature-enhanced images resulted in higher recognition rates. We have also conducted reduced-resolution data experiments, and used the feature-based classifier to test the performance of feature-enhanced, superresolution images. We have observed recognition improvements as compared to the conventional images in this case, as well. Table 5 summarizes the results obtained in this paper in terms of the probability of correct classification.

	T72	BMP2	BTR70
T72	159	30	7
BMP2	53	120	22
BTR70	33	32	131

(a) Conventional images. $P_{cc} = 69.85\,\%$

	T72	BMP2	BTR70
T72	176	13	7
BMP2	8	173	14
BTR70	3	20	173

(b) Point-enhanced images. $P_{cc} = 88.93\,\%$

	T72	BMP2	BTR70
T72	184	11	1
BMP2	3	191	1
BTR70	1	2	193

(c) Region-enhanced images. $P_{cc} = 96.76\,\%$

Table 2. Confusion matrices summarizing the template-based classification results. The entry in row i, column j shows the number of images from vehicle type i classified as vehicle j.

	T72	BMP2	BTR70
T72	170	18	8
BMP2	7	161	27
BTR70	4	12	180

(a) Conventional images. $P_{cc} = 87.05\,\%$

	T72	BMP2	BTR70
T72	190	5	1
BMP2	10	178	7
BTR70	8	2	186

(b) Point-enhanced images. $P_{cc} = 94.38\,\%$

	T72	BMP2	BTR70
T72	193	3	0
BMP2	1	194	0
BTR70	1	0	195

(c) Region-enhanced images. $P_{cc} = 99.15\,\%$

Table 3. Confusion matrices summarizing the likelihood-based classification results. The entry in row i, column j shows the number of images from vehicle type i classified as vehicle j.

ACKNOWLEDGMENTS

This work was supported by the Army Research Office under Grants DAAD19-00-1-0466 and DAAG55-97-1-0013, the Office of Naval Research under Grant N00014-00-1-0089, the Air Force Office of Scientific Research under Grant F49620-96-1-0028, and the National Institutes of Health under Grant NINDS 1 R01 NS34189.

REFERENCES

1. M. Çetin and W. C. Karl, "Feature-enhanced synthetic aperture radar image formation based on non-quadratic regularization," *IEEE Trans. Image Processing* **10**, pp. 623–631, Apr. 2001.
2. M. Çetin, W. C. Karl, and D. A. Castañon, "Evaluation of a regularized SAR imaging technique based on recognition-oriented features," in *Algorithms for Synthetic Aperture Radar Imagery VII*, E. G. Zelnio, ed., *Proc. SPIE* **4053**, pp. 40–51, (Orlando, FL, USA), Apr. 2000.

	T72	BMP2	BTR70
T72	38	84	74
BMP2	14	114	67
BTR70	4	81	111

(a) Conventional images. $P_{cc} = 44.80\,\%$

	T72	BMP2	BTR70
T72	162	23	11
BMP2	28	147	20
BTR70	10	17	169

(b) Point-enhanced, superresolution images. $P_{cc} = 81.43\,\%$

Table 4. Confusion matrices summarizing the point-feature-based classification results, from reduced-resolution data. The entry in row i, column j shows the number of images from vehicle type i classified as vehicle j.

High-resolution, low-SNR experiment			
	Conventional	Point-Enhanced	Region-Enhanced
Template-based classifier	69.85 %	88.93 %	96.76 %
Likelihood-based classifier	87.05 %	94.38 %	99.15 %

Reduced-resolution, high-SNR experiment		
	Conventional	Point-Enhanced, Superresolution
Point-feature-based classifier	44.80 %	81.43 %

Table 5: Overall summary of the classification experiments, in terms of the probability of correct classification, P_{cc}.

3. "Air Force Research Laboratory, Model Based Vision Laboratory, Sensor Data Management System MSTAR Web Page: http://www.mbvlab.wpafb.af.mil/public/sdms/datasets/mstar/."
4. C. V. Jakowatz Jr., D. E. Wahl, P. H. Eichel, D. C. Ghiglia, and P. A. Thompson, *Spotlight-mode Synthetic Aperture Radar: a Signal Processing Approach*, Kluwer Academic Publishers, Norwell, MA, 1996.
5. D. Geman and G. Reynolds, "Constrained restoration and the recovery of discontinuities," *IEEE Trans. Pattern Anal. Machine Intell.* **14**, pp. 367–383, Mar. 1992.
6. C. R. Vogel and M. E. Oman, "Fast, robust total variation-based reconstruction of noisy, blurred images," *IEEE Trans. Image Processing* **7**, pp. 813–824, June 1998.
7. L. M. Novak, G. J. Owirka, W. S. Brower, and A. L. Weaver, "The automatic target-recognition system in SAIP," *Lincoln Laboratory Journal* **10**(2), pp. 187–202, 1997.
8. G. J. Owirka, S. M. Verbout, and L. M. Novak, "Template-based SAR ATR performance using different image enhancement techniques," in *Algorithms for Synthetic Aperture Radar Imagery VI*, E. G. Zelnio, ed., *Proc. SPIE* **3721**, pp. 302–319, (Orlando, FL, USA), Apr. 1999.
9. J. A. O'Sullivan, M. D. Devore, V. Kedia, and M. I. Miller, "SAR ATR performance using a conditionally Gaussian model," *IEEE Trans. Aerosp. Electron. Syst.* . Submitted for publication.
10. G. Jones, III and B. Bhanu, "Recognition of articulated and occluded objects," *IEEE Trans. Pattern Anal. Machine Intell.* **21**, pp. 603–613, July 1999.
11. W. W. Irving and G. J. Ettinger, "Classification of targets in synthetic aperture radar imagery via quantized grayscale matching," in *Algorithms for Synthetic Aperture Radar Imagery VI*, E. G. Zelnio, ed., *Proc. SPIE* **3721**, pp. 320–331, (Orlando, FL, USA), Apr. 1999.
12. M. Hazlett, D. J. Andersh, S. W. Lee, H. Ling, and C. L. Yu, "XPATCH: a high-frequency electromagnetic scattering prediction code using shooting and bouncing rays," in *Targets and Bachgrounds: Characterization and Representation*, W. R. Watkins and D. Clement, eds., *Proc. SPIE* **2469**, pp. 266–275, (Orlando, FL, USA), Apr. 1995.